Fusion Dynamics of Hybrid Cell–Microparticle Aggregates: A Jelly Pearl Model

Grégory Beaune, Laura Sinkkonen, David Gonzalez-Rodriguez, Jaako V. I. Timonen, Françoise Brochard-Wyart

Fusion dynamics of hybrid cell-microparticles aggregates: a jelly pearl model

Grégory Beaune,[1] Laura Sinkkonen,[1] David Gonzalez-Rodriguez,[2,#] Jaakko V.I. Timonen,[1,#] Françoise Brochard-Wyart[3,#,*]

[1] Department of Applied Physics, Aalto University School of Science, Puumiehenkuja 2, 02150, Espoo, Finland

[2] Université de Lorraine, LCP-A2MC, F-57000, Metz, France

[3] Institut Curie, Université PSL, Sorbonne Université, CNRS UMR168, Laboratoire Physico Chimie Curie, 75005, Paris, France

[#] Equally contributors

* Corresponding author. Email address: Francoise.Brochard@curie,fr

Abstract.

We study the fusion of homogeneous cell aggregates and of hybrid aggregates combining cells and microparticles. In all cases we find that the contact area does not vary linearly over time, as observed for liquid drops, but rather it follows a power law in $t^{2/3}$. This result is interpreted by generalizing the fusion model of soft viscoelastic solid balls to viscoelastic liquid balls, akin to jelly pearls. We also explore the asymmetric fusion between a homogeneous aggregate and a hybrid aggregate. This latter experiment allows determining the self-diffusion coefficient of the cells in a tissue by following the spatial distribution of internalized particles in the cells.

1. Introduction.

Cellular aggregates are an essential and a widely used in vitro tissue model that has supported fundamental advances in the biophysical understanding of developing and pathological tissues and opened up new therapeutical perspectives.[1–3] Many of these studies have their foundation on Malcolm Steinberg's seminal work on the Differential Adhesion Hypothesis,[4,5] which establishes an analogy between a soft tissue as an assembly of interacting cells, and a viscous liquid drop as an assembly of interacting molecules. Same as in a liquid drop, geometrical imbalance of cellular adhesive interactions at the aggregate surface gives rise to a surface tension that powers tissue sorting and self-assembly. This view of tissues is not exempt of controversy, since the simplicity that makes the analogy powerful disregards certain aspects of biological tissue complexity. For example, some groups have advocated for more complex views of tissues as visco-elasto-plastic solids.[6,7] In spite of such objections, Steinberg's avant-garde hypothesis continues to feed current research and remains relevant today.

Different techniques have been developed to characterize the properties of soft tissues and cellular aggregates. With the spreading technique,[8,9] the aspiration inside a pipette,[10,11] and the compression between two parallel plates,[12,13] the fusion is a technique of choice to determine the mechanical properties of viscoelastic materials and especially of cellular aggregates. Using these different techniques, we can determine their surface tension γ, rigidity E, and viscosity η. Beyond mechanical characterization, fusion between two tissues is a fundamental biophysical phenomenon that constitutes an essential step in embryonic development and disease progression,[14] and that provides the basic mechanism of bioprinting, where cell aggregates are used as building blocks whose coalescence and self-assembly yields the desired artificial tissue structures.[15–17] The fusion experiment consists in putting in contact two cellular aggregates of similar size and monitor their dynamics of coalescence over time. The characteristic time τ over which coalescence takes place is called the relaxation time. At long time, typically over several days, the two cell aggregates typically fuse completely to yield one final spherical aggregate, although a phenomenon of arrested coalescence has been described for certain cell aggregate types, as discussed below.

Models of aggregate fusion take up the sintering theory of viscous liquid droplets, which was started by the work of Frenkel.[18,19] Frenkel's sintering model considers the balance between surface tension and viscous dissipation, under a geometrical approximation of small deformation, valid for short times. This approach yields the dynamics equation $\frac{a^2}{R_0} = \frac{\gamma}{\eta} t$, where a is the radius of the neck joining the two drops, R_0 is the initial drop radius, and γ/η is the visco-capillary velocity, corresponding to a characteristic fusion time $\tau_f \sim \eta R_0/\gamma$. The original Frenkel model was corrected by Eshelby to satisfy the continuity equations.[20] Later, Pokluda et al. extended the Frenkel-Eshelby model to account for an increase in drop radius over time owing to volume conservation, thus obtaining an expression that is valid over a longer time range.[21] While these models are based on simplifying assumptions on the flow field inside the aggregates, more detailed descriptions have been obtained by solving the exact flow equations, either analytically for a 2D geometry[22] or numerically for a 3D axisymmetric[23–25] or a fully 3D geometry.[26]

Motivated by the study of polymeric liquids, more recent works investigated the coalescence of viscoelastic rather than viscous droplets. The adhesion of two elastic polymer beads is described by the well-known Johnson-Kendall-Roberts (JKR) model,[27] which characterizes the final equilibrium shape. The kinetics to reach this equilibrium of this process were first described by Michel and Shanahan in an insightful article,[28] which has not received the

attention it deserves, perhaps because it was written in French. Later studies experimentally characterized viscoelastic effects in polymer coalescence.[29,30] Mazur and Plazek[31] theoretically described viscoelastic sintering by means of a modified JKR model with a time-dependent compliance, while later studies developed numerical simulations based on upper-convected Maxwell models[30,32–34] or other rheological models of viscoelasticity.[35] The overall picture arising from these studies depicts three regimes of viscoelastic sintering:[33] a first zipping regime at very short times dominated by direct Van der Waals attraction,[32] which interestingly has also been described for cellular aggregates;[36] a second regime dominated by viscoelasticity and consistent with JKR theory;[33] and a long-time regime dominated by viscosity.[33,34]

The Frenkel-Eshelby model of viscous sintering has been applied in different studies to describe the initial stages of cell aggregate fusion, over times of up to several hours, in order to estimate the cell aggregate visco-capillary parameter, γ/η.[12,37–40] Moreover, the improved model proposed by Pokluda et al.[21] has been reported to successfully describe aggregate fusion over several hours, and to be in agreement with numerical simulations over longer times.[41] These studies do not consider aggregate growth over time since they assume incompressible droplets. However, when the time scale of fusion is larger than that of cell division, which is often the case with cancerous cellular aggregates, cell proliferation needs to be accounted for. This case has been addressed by Dechristé et al.[42] by extending the viscous sintering model to account for cell division.

The above theoretical models treat cell aggregates as viscous drops and disregard the effects of viscoelasticity. Only very recently has viscoelastic aggregate fusion been first considered,[43,44] most notably to explain the experimentally observed phenomenon of arrested coalescence,[45–47] where certain types of cellular aggregates do not appear to fuse completely but rather to stabilize at a state of partial fusion. Arrested coalescence has been explained by describing the aggregate as an incompressible Kelvin-Voigt viscoelastic solid,[43] or by adding an elastic term to Pokluda et al.'s viscous sintering model.[44] The final state is thus found to depend on the parameter $\beta=ER_0/\gamma$, i.e., the ratio of elasticity to surface tension, with arrested coalescence appearing when elasticity is dominant.[43] Alternatively, the arrested coalescence phenomenon has also been described by numerical simulations considering individual cell activity, which show a transition from arrested coalescence to complete fusion with increasing activity.[43,44] In a very recent contribution, Kosheleva et al.[48] have also questioned the validity of the viscous liquid model of aggregate fusion from a different perspective. While Kosheleva et al. obtain a reasonable fit between the Frenkel-Eshelby model and their experimental results for different aggregate types, the fitted visco-capillary velocities γ/η are inconsistent with previous

experimental findings for similar cell types, and they significantly depend on the age of the aggregates (3 or 7 days). This leads Kosheleva et al. to postulate an important role of the extracellular matrix present in the aggregates on their fusion dynamics.

A common feature between the Frenkel-Eshelby viscous model and the more recent viscoelastic descriptions introduced to explain arrested coalescence is their common prediction of a short-time dynamics that scale as $a \sim t^{1/2}$. This scaling arises from assuming that the viscous or viscoelastic response occurs at the scale of the complete aggregate, a volume of order R_0^3. Such assumption is in contrast with the kinetic model of Michel and Shanahan based on JKR theory, where viscous dissipation at short time occurs only within the region of significant elastic deformation, of order a^3. The Michel-Shanahan scaling was shown to correctly predict the spreading of the cellular aggregate onto a substrate,[8] a phenomenon closely resembling aggregate fusion. These considerations bring us here to apply the Michel-Shanahan model of the kinetics of the JKR experiment to describe the fusion of cellular aggregates, and show that this JKR-MS model, rather than the widely used Frenkel-Eshelby model, correctly predicts our experimentally observed dynamics of aggregate fusion. It is also remarkable that Michel and Shanahan's argument can be transposed to describe the spreading of soft elastic shells, in particular the spreading of biomimetic actin cortices[49] and single cells[50,51].

2. **Experimental materials and methods**

- Materials

Water (18.2 MΩ cm) was deionized using a Milli-Q water purification system (Millipore). The fluorescent polystyrene particles (FluoSpheres®) were purchased from Thermo Fischer Scientific Co and will be referred to as microparticles (MPs). Their diameters, provided by the supplier, were 9.90 ± 0.12 µm (carboxylated polystyrene). Particles were labeled with a proprietary dye (λ_{max}= 540 nm, $\lambda_{max,\,fl}$ = 560 nm). Dulbecco's Modified Eagle's Medium (DMEM, Gibco®), Fetal Bovine serum (FBS, Gibco®), and penicillin-streptomycin (Gibco®) were obtained from Thermo Fischer Scientific Co. Fibronectin was purchased from Sigma-Aldrich.

- Cell culture and formation of cellular aggregates

We used murine sarcoma (S180) cells transfected to express different amount ϕ of E-cadherins molecules on their surface[52], thereby controlling the intercellular adhesion energy. We used ϕ

= 48% and 100%, where the most adhesive cell line is defined as ϕ = 100%.[8] These cell lines were a generous gift from Dr. Sylvie Dufour (INSERM, U955, France).

Cells were cultured at 37 °C under a 95% air/5% CO_2 atmosphere in a culture medium consisting of DMEM supplemented with 10% (v/v) FBS and antibiotics (100 µg ml^{-1} streptomycin and 100 U ml^{-1} penicillin).

Cell/MP aggregates were prepared using the hanging droplet method[53]. Upon reaching confluence, cells were detached from the flask using trypsin and dispersed into DMEM with a concentration of 4.10^5 cells ml^{-1}. MPs were added to the cells to reach the desired concentration by varying the initial volume fraction φ_i of MPs in the hanging droplets ($\varphi_i = \frac{volume\ of\ MPs}{volume\ of\ MPs + volume\ of\ cells}$, with $0 \leq \varphi_i \leq 0.7$). The volume fractions have been calculated considering a volume per single cell equal to 1600 µm^3.

Droplets (15 µl) of the cell/MP suspension in cell culture medium were deposited on the lid of a Petri dish. The lid was inverted and placed on top of a Petri dish filled with distilled water, such that the droplets containing the cells in the medium and hanging from the lid were maintained under a high humidity atmosphere. Due to gravity, cells fell to the bottom of the droplets and started to adhere to each other to form clusters of cells. After 2 days of incubation, cell aggregates were formed. For experiments with cells alone (φ_i = 0), the same protocol was followed except that the addition of MPs was omitted.

As expected, cell aggregates prepared with cells ϕ = 100% (stronger cell-cell interactions) have a smoother surface than cell aggregates prepared with cells ϕ = 48%, where the cell-cell interactions are lower.

- Confocal microscopy

Cell aggregates were imaged and recorded by confocal microscopy (LSM 710, 20×/1.0 water immersion objective, λ_{ex} = 488 nm and λ_{em} = 490 – 530 nm for E-cadherin, λ_{ex} = 561 nm and λ_{em} = 463 – 735 nm for MPs).

Images were exported from the instrument software (Zeiss Zen Black) in CZI format and further processed with Fiji (version 1.53c).

- Fusion experiments

Two aggregates of similar size are placed in contact in an observation chamber. The observation chamber is a cylindrical sample cell (magnetic chamber, Chamlide), whose bottom

part is a glass coverslip. To prevent adhesion of the cells to the glass, non-adhesive glass substrates are prepared.

To do so, 25-mm circular glass coverslips were plasma cleaned for 5 min (Henniker plasma, HPT-100). PEG-PLL coating was performed using a 0.1 mg ml^{-1} Polyethylene glycol polylysin (PLL(20)-g[3.5]-PEG(2), Surface Solution, Dubendorf, Switzerland) in HEPES solution (pH 7.3, 0.1 M) for one hour. Coverslips were then rinsed with Phosphate Buffer Solution (PBS, pH 7.4).

The chamber is filled with CO_2-equilibrated culture medium. The chamber is maintained at 37 °C using a temperature-controlled platform (Pecon Incubation insert P-SET 2000) connected to a thermostat (Lausa Eco Gold) and the atmosphere is kept at 5% of CO_2 either connecting the platform to a CO_2 bottle or pouring silicone oil on top of the medium. Aggregates are then suspended in the observation chamber and aggregates with similar size are manually paired with a disposable pipette tip. The fusion of aggregates is monitored using the microscope and software mentioned earlier and pictures are recorded with a 5 min interval for at least 16h.

3. Theoretical models

In this section we start by presenting the classic Frenkel-Eshelby model of viscous sintering, largely used to describe cell aggregate fusion. Next, we present the viscoelastic model first introduced by Michel and Shanahan[28] to quantify the kinetics of JKR adhesion, and which here we apply to describe viscoelastic fusion.

3.1 *Viscous* fusion model

The Frenkel-Eshelby model can be summarized in the following simple argument. Let us consider two fusing aggregates of identical initial radius R_0. At time t after the beginning of the fusion, the aggregates have radius R and they contact each other at a circular surface of neck radius a and area πa^2. A simple geometric inspection tells us that the aggregate indentation length is $\delta \approx a^2/R$. The Frenkel-Eshelby model assumes that the whole aggregate is deformed by this indentation, thus the deformation scales as $\varepsilon \approx \delta/R \approx a^2/R^2$. The dynamics of deformation result from a balance between frictional loses due to viscous flow in the whole aggregate and surface energy:

$$\eta \dot{\varepsilon}^2 R^3 \approx \gamma a \dot{a}, \qquad (1)$$

where η is the aggregate viscosity and γ its surface tension. Accounting for numerical factors and assuming $R \approx R_0$ throughout the whole fusion process, Eq. 1 leads to an exponential evolution of the neck radius $a(t)$, which at short times can be approximated by the original Frenkel-Eshelby expression,

$$a^2 = \frac{\gamma}{\eta} R t, \tag{2}$$

i.e., a neck radius that increases with time as $t^{1/2}$.

3.2 *Viscoelastic* fusion model

According to JKR theory,[27] deformation of an adhesive elastomer is concentrated at a region whose volume scales as a^3. In the viscoelastic model of Michel and Shanahan,[28] the viscous flow field is imposed by the elastic deformation and thus viscous dissipation is concentrated in this same region and involves a local friction coefficient η_1. This argument leads to a deformation that scales as $\varepsilon \approx \delta/a \approx a/R$. Balance between viscous dissipation and adhesion now yields

$$\eta_1 \dot{\varepsilon}^2 a^3 \approx \gamma a \dot{a} \tag{3}$$

$$\eta_1 \left(\frac{\dot{a}}{R}\right)^2 a^3 \approx \gamma a \dot{a}. \tag{4}$$

Accounting for elastic energy and for numerical factors, the governing differential equation reads:[28]

$$\frac{m a^2 \eta_1}{3R} \frac{\mathrm{d}a}{\mathrm{d}t} = \frac{3\pi R W}{2} - \frac{K a^3}{R}, \tag{5}$$

where $K = 8E/9$ for two contacting aggregates, with $W=2\gamma$ the adhesion energy per unit surface, E the rubber elastic modulus, and $m \approx 10$ is a constant involved in the scaling of the effective volume of deformation. The numerical factors in Eq. 5 account for the presence of two spheres, unlike the original Michel and Shanahan equation, which was derived for a sphere on a flat rigid substrate. Eq. 5 leads to an exponential evolution law,

$$a^3 = L_e R^2 \left(1 - e^{-t/\tau_1}\right), \tag{6}$$

where $L_e = \frac{3\pi W}{2K} = \frac{27\pi}{8}\frac{\gamma}{E} \sim 10\frac{\gamma}{E}$. L_e is the elastic length, which describes the competition between the deformation energy of the soft matrix and the surface energy.[54] For classical rubber, $E \sim 10^6$ Pa and $L_e \sim 10$ nm. For ultra-soft rubbers and tissues, $E \sim 10^3$ Pa and $L_e \sim 10$ μm. $\tau_1 = \frac{m\eta_1}{9K} = \frac{m\eta_1}{8E} \sim \frac{\eta_1}{E}$ is the rubber relaxation time. At short time, Eq. 6 can be approximated by

$$a^3 = L_e R^2 \frac{t}{\tau_1} = C \frac{\gamma}{\eta_1} R^2 t, \qquad (7)$$

with $C = 27\pi/(2m)$ a numerical constant. Thus, the Michel-Shanahan model predicts an increase of neck radius that scales as $t^{1/3}$, instead of $t^{1/2}$ as predicted by the Frenkel-Eshelby model. The characteristic time of fusion τ_f is obtained by making $a = R$ in Eq. 7, which yields $\tau_1 \sim R\eta_1/\gamma$, the same scaling as in the Frenkel-Eshelby model.

We notice that Eq. 6 yields a final equilibrium state $a_{max}^3 = L_e R^2$, which can be smaller than the complete fusion state ($a = R$) if $L_e < R$. This is the case of arrested fusion for aggregates behaving as viscoelastic solids, as discussed by Oriola et al.[43] In our experiments, we systematically observe viscoelastic liquid behavior, with fused aggregates achieving a spherical shape for sufficiently long times. In order to describe a viscoelastic liquid behavior, rather than a solid one, we consider that the elastic stress in the aggregate is relaxed at long times via cell rearrangements, as we discuss in what follows.

3.3 *Viscoelastic liquid* fusion model

Here we extend the Michel-Shanahan model to account for long-time liquid behavior. We adopt a well-established rheological model for cellular aggregates[10] consisting of a Kelvin-Voigt model, which represents cell viscoelasticity, in series with a damper, which represents tissue viscosity. The rheological model is depicted in Fig. 1. The Kelvin-Voigt element is characterized by constants λKa and $\mu\eta_1 a$, and the damper in series has a constant $\mu\eta_t a$, where $K = 8E/9$ is the elastic constant, η_1 is the cell viscosity, η_t is the tissue viscosity, a is the neck radius of aggregate contact, and λ and μ are numerical constants whose values we will set below.

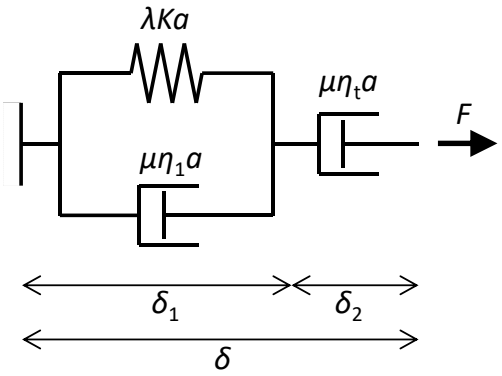

Fig 1. Rheological model of a cellular aggregate. Aggregate rheology is described by a Kelvin-Voigt model of constants λKa and $\mu\eta_1 a$ representing cell viscoelasticity in series with

a damper of constant $\mu\eta_t a$ representing tissue viscosity. Upon application of a force F, the system length varies by an amount $\delta = \delta_1 + \delta_2$.

Under the action of a force F, the length of the system varies by an amount $\delta = \delta_1 + \delta_2$, the sum of the contributions of the Kelvin-Voigt element and the additional damper. These variables are related by

$$\frac{F}{a} = \lambda K \delta_1 + \mu\eta_1 \dot{\delta}_1 = \mu\eta_\mathrm{t} \dot{\delta}_2. \tag{8}$$

By combining Eq. 8 with its time derivative, we obtain an equation relating F and δ:

$$\frac{\lambda K}{\mu\eta_\mathrm{t}} \frac{F}{a} + \left(1 + \frac{\eta_1}{\eta_\mathrm{t}}\right) \frac{\mathrm{d}}{d\mathrm{t}} \left(\frac{F}{a}\right) = \lambda K \dot{\delta} + \mu\eta_1 \ddot{\delta}. \tag{9}$$

In the limit $\eta_\mathrm{t} \to \infty$, Eq. 9 yields $F = \lambda K a\delta + \mu\eta_1 a\dot{\delta}$. In this limit, we should retrieve the force-displacement relation in Michel and Shanahan's model, which requires choosing $\lambda = 3/2$ and $\mu = m/4$.

The fusion dynamics is governed by the balance between the rate of change in the adhesion energy $U_\mathrm{adh} = \pi a^2 W$, with $W = 2\gamma$ the adhesion energy per unit surface, and the work done by the force F. This energy balance reads $\dot{U}_\mathrm{adh} = 2F\dot{\delta}$, where the factor of 2 accounts for the deformation of both aggregates. Aggregate indentation is governed by JKR theory and thus $\delta = 2a^2/(3R)$ for two contacting spheres of equal radius R. By treating the aggregate radius R as a constant, the energy balance leads to

$$F = \frac{3}{2}\pi R W, \tag{10}$$

i.e., a constant force. This result allows us to rewrite Eq. 9 as:

$$\mu\eta_1 \ddot{\delta} + \left[\lambda K + \left(1 + \frac{\eta_1}{\eta_\mathrm{t}}\right) \frac{F}{\sqrt{6R}} \delta^{-3/2}\right] \dot{\delta} - \frac{\lambda K F}{\mu\eta_\mathrm{t}\sqrt{3R/2}} \delta^{-1/2} = 0, \tag{11}$$

which is the differential equation governing aggregate fusion. At short time, $\delta_1 \gg \delta_2$ and the dynamics is governed by the Kelvin-Voigt element. Thus, we obtain

$$a^3 = a_\mathrm{e}^3 \left(1 - e^{-t/\tau_1}\right) \approx \frac{27\pi R^2 W}{2m\eta_1} t, \tag{12}$$

where $\tau_1 = m\eta_1/(9K)$ and

$$a_\mathrm{e}^3 = \frac{3\pi W R^2}{2K} = L_e R^2, \tag{13}$$

where L_e is the elastic length $L_e = 3\pi W/(2K) = 27\pi\gamma/(8E)$. With $\gamma \approx 6.10^{-3}$ Nm^{-1} and $E \approx 700$ Pa,[10] we estimate $L_\mathrm{e} \approx 90$ μm.

We note that the asymptotic short-time solution, Eq. 12, corresponds to Michel and Shanahan's result (Eq. 7 above). At long time, the dynamics is governed by that of the additional damper and we can write $F/a \approx \mu\eta_t\dot{\delta}$, which leads to

$$a^3 = L_e R^2 + L_e R^2 \frac{t}{\tau_t}, \tag{14}$$

where $\tau_t = \frac{m\eta_t}{9K}$.

Therefore, we predict that Michel and Shanahan's scaling $a \sim t^{1/3}$ is valid both at short and at long times, except of course at the very final times of the fusion, where the approximation of constant R is no longer valid. We note that, if the aggregate radius is small, fusion is completed in the short-time regime. This corresponds to the case where $a_e > R$, which corresponds to $L_e > R$. For small aggregates such that $R < L_e$, we can describe the fusion by the simplified relation in Eq. 12, which yields a characteristic fusion time $\tau_{f,1} = 2m\eta_1 R/(27\pi W)$. For large aggregates such that $R > L_e$, we must consider both regimes. The two asymptotic expressions at short and long times, Eqs. 12 and 14, can be combined in the following approximate solution for all times:

$$\frac{a^3}{R^2} \approx \frac{3\pi W}{2K}\left(1 - e^{-t/\tau_1}\right) + \frac{27\pi W}{2m\eta_t} t \approx L_e\left(1 - e^{-t/\tau_1}\right) + \frac{L_e}{\tau_t} t, \tag{15}$$

where $\tau_1 = \frac{m\eta_1}{9K}$, $\tau_t = \frac{m\eta_t}{9K}$, and $V_f^* = \frac{L_e}{\tau_t} = \frac{27\pi W}{2m\eta_t}$ is a characteristic fusion velocity. The characteristic fusion time for large aggregates ($R > L_e$) is thus $\tau_{f,2} = 2m\eta_t R/(27\pi W)$. Fig. 2a shows a comparison between the numerical solution to Eq. 11 and the approximation given by Eq. 15. The agreement is reasonable except when $a \gg a_e$, because in this regime the elastic deformation $\delta_1 \to 0$ as a result of the progressive increase of the contact region a and of the effective elastic constant $\lambda K a$. We thus expect the short-time elastic deformation of the spring to exponentially vanish over a characteristic time of the order of η_t/K. Based on this idea, we try to fit the numerical solution by the following semi-empirical expression:

$$\frac{a^3}{R^2} \approx L_e\left(1 - e^{-t/\tau_1}\right) e^{-\frac{\alpha K}{\eta_t} t} + L_e \frac{t}{\tau_t} \tag{16}$$

We find that a good approximation is obtained for $\alpha = 0.3$, as shown in Fig. 2b.

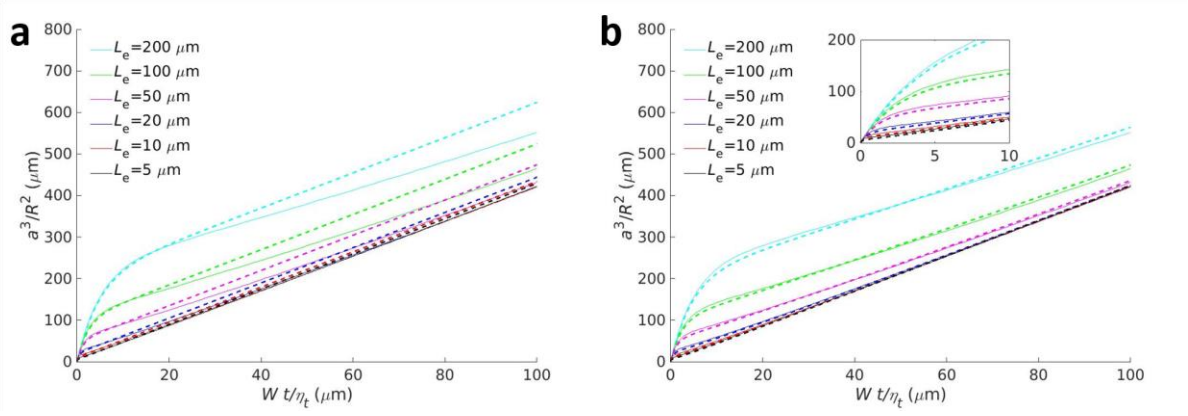

Fig 2. Predicted dynamics of viscoelastic liquid fusion. (a) Comparison between the numerical solution of the ODE (Eq. 11, full lines) and the approximate solution (Eq. 15, dashed lines). (b) Comparison between the numerical solution of the ODE (Eq. 11, full lines) and the semi-empirical approximation (Eq. 16, dashed lines). Calculations are performed with $\eta_t/\eta = 10$, m = 10, and for different values of the elastic length, L_e. The inset shows a magnification of the short-time regime.

4. Results and discussion

- Formation of cellular aggregates

We study the fusion of cellular aggregates formed of different types of cells and MPs. We use two types of cells that express different levels of E-cadherin on their surface, controlling the cell-cell interactions. The cells expressing the highest E-cadherin level are referred to as ϕ = 100% (most adhesive cell line), and those expressing half this amount of E-Cadherin are referred to as ϕ = 48%.

The MPs are fluorescent polystyrene microparticles with a diameter of 10 µm. Aggregates with different MP concentrations are obtained by screening the total number of objects per hanging droplet (e.g. cells and MPs) and the ratio of cells and MPs in order to include a large number of MPs in the final aggregates (Table 1).

We prepare cellular aggregates with and without MPs using the hanging droplet method. Cell aggregates prepared with MPs are referred as hybrid aggregates. We add the desired number of cell and MPs (see Table 1) per droplet and the aggregates are allowed to form for two days. After this period of time, hybrid cellular aggregates are observed with a confocal microscope and Z-stacks are performed. Because the aggregates absorb the visible light, the intensity of the MPs decreases as Z increases until it completely disappears when the core of the aggregates are reach. Using the Z-stacks we count the number of MPs in the first 80-100 µm of the hybrid

aggregates and by comparison of the volume of the aggregates for the same Z-stack we approximate the volume fraction of MPs in the aggregates (Table 1). Notice that the measured particle volume fraction is four times smaller than the initial volume fraction in the pendant droplet, which can be attributed to cell division (Supplementary Table 1).

Hybrid aggregates prepared with cells ϕ = 100% are smaller than the ones prepared with ϕ = 48%, while the total volume of objects put in hanging droplets is similar.

Hybrid aggregates formed with cells ϕ = 100% include more MPs than the ones formed with ϕ = 48%. The distribution of MPs in the aggregates is imaged by confocal microscopy, as shown in Fig. 3. We observe either single or few MPs internalized by the cells and larger clusters located outside the cells.

Table 1. Number of cells and MPs for each type of MPs and volume fractions of the different types of aggregates.

E-cadherin expression ϕ (%)	Number of cells per droplet	Number of MPs per droplet	Volume fraction of MPs in an aggregate
48	1100	0	0
48	550	1650	0.06
100	1000	0	0
100	570	1890	0.10
100	285	1890	0.12

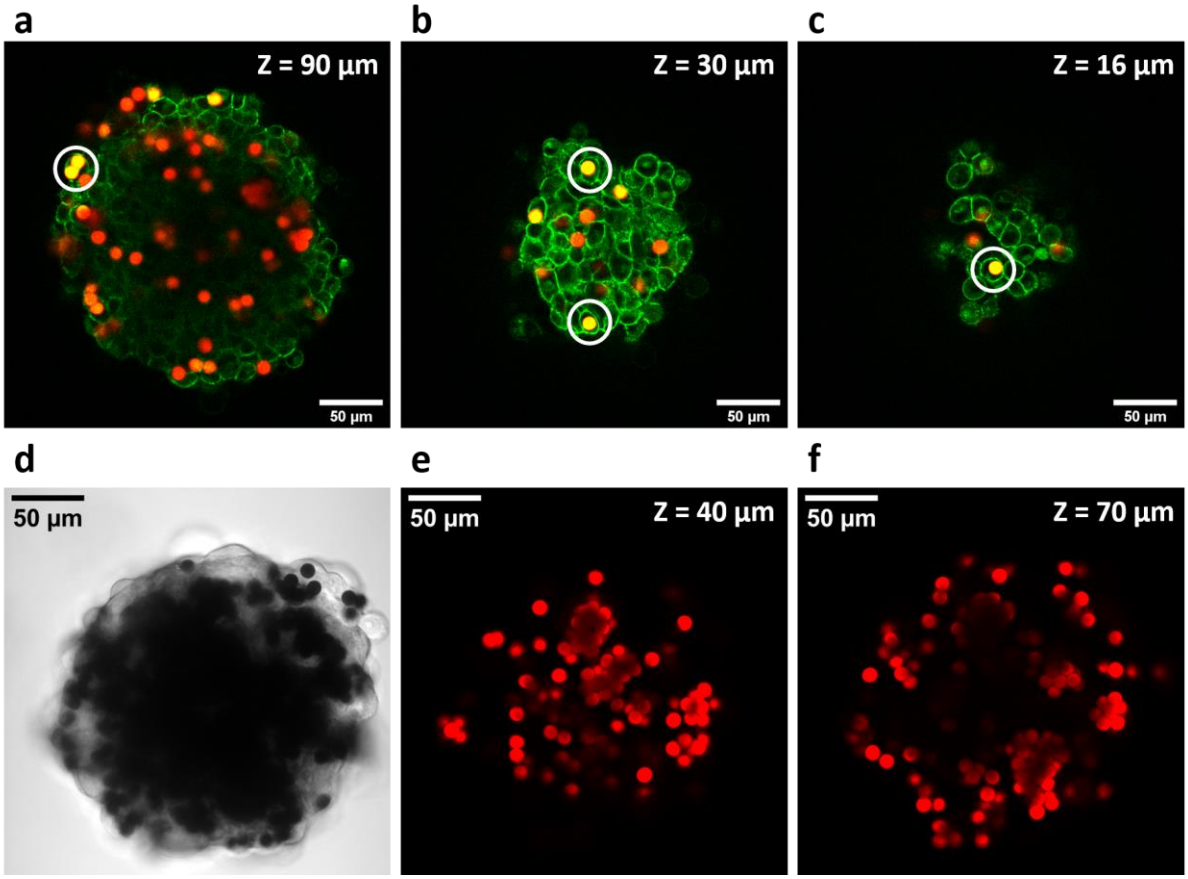

Fig 3. Location of MPs in hybrid aggregates. Hybrid aggregates after 2 days of incubation in hanging droplets. (a-c) Hybrid aggregate with ϕ = 48% and φ = 0.06. Confocal sections at (b) Z = 30 µm and (c) Z = 16 µm with E-cadherin in green and MPs in yellow and red. Examples of MPs located inside cells are circled in white. (d-f) Hybrid aggregates with ϕ = 100% and φ = 0.12. (d) Bright field picture, (e) confocal section at Z = 40 µm and (f) at Z = 70 µm. MPs are visible in red.

- Fusion of homogeneous cellular aggregates

We study the effect of cell-cell interactions on the fusion of cell aggregates by comparing the fusion of pairs of cell aggregates made of cells expressing ϕ = 48% E-cadherin (Fig. 4a) and pairs of aggregates made of cells expressing ϕ = 100% E-cadherin (Fig. 4c).

During fusion, the cell aggregates are connected by a neck of radius a that increases over time. Fig. 4b,d shows log a as a function of log t and the analysis indicates that this representation can be fitted with the function $\log a = p.\log t + q$. The obtained values are in Table 2 and in agreement with the viscoelastic prediction p = 0.33. We can notice slightly higher slope values for stronger cell-cell interactions. We can compare the experimental values of q~0.8 to the theoretical prediction $q = \frac{1}{3}\log\frac{L_e R^2}{\tau_t}$. With L_e~20 µm and R~10^2 µm, we get τ_t~4.10^3 s, in

good agreement with [10]. Fig. 4e,f shows a^3/R^2 as a function of t. The fit with eq 15 leads to a measurement of L_e and V_f*. The obtained values are in Table 2, showing that L_e and V_f* decreases from 30 to 10 μm and 3 to 2 μm s^{-1}, respectively, as the E-Cadherin expression increases from 48 to 100%. L_e is comparable to the cell size, which explains the large dispersion of the results for L_e. It is noted that the values reported in Table 2 correspond to a fit of the approximate solution, Eq. 15. An alternative procedure is a direct, numerical fit of the differential equation (Eq. 11), which can be easily performed with common scientific packages. For some cases, this alternative procedure leads to different estimates, because the exact solution of Eq. 11 somewhat differs from the approximate solution of Eq. 15 at long times, as shown in Fig. 2 above. Qualitatively, both fitting procedures lead to the same conclusions, so we choose to discuss our experiments based on a fit of the approximate solution, which provides better physical insight into the asymptotic behaviors.

Since the cell lines used in this study divide approximately in 18 h, the volume of cell aggregates increases noticeably after more than one day of fusion. Therefore, we have also analyzed the fusion kinetics on a shorter time scale of up to t = 9 hours and found that the values of p and q are practically unchanged (Supplementary Table 3).

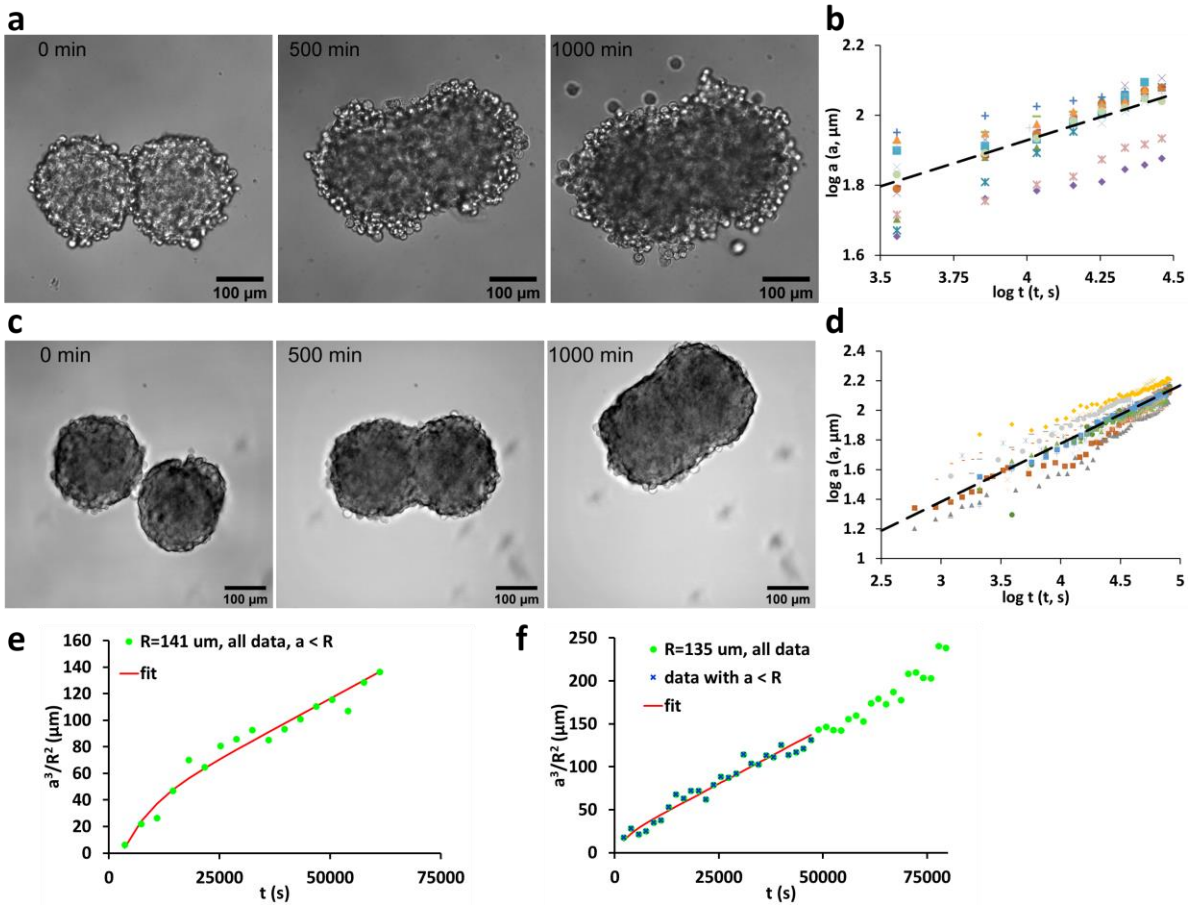

Fig 4. Fusion of cell aggregates with different cell-cell interactions. (a) Pictures of the fusion of a pair of cell aggregates at t = 0, 500 and 1000 min with ϕ = 48%. (b) Plot of log a as a function of log t of cell aggregates with ϕ = 48%, n = 6. The fuzzy edge of the cellular aggregates makes it difficult to visualize the fusion neck at short time. (c) Pictures of the fusion of a pair of cell aggregates at t = 0, 500 and 1000 min with ϕ = 100%. (d) Plot of log a as a function of log t of cell aggregates with ϕ = 100%, n = 14. Doted lines correspond to linear fits. (e) Plot of a^3 / R^2 as a function of t for cell aggregates with ϕ = 48% and theoretical fit using Eq. 15. (f) Plot of a^3 / R^2 as a function of t for cell aggregates with ϕ = 100% and theoretical fit using Eq. 15.

- Fusion of hybrid aggregates

We investigate the fusion of pairs of hybrid aggregates containing cells and microparticles. Fig. 5 shows the fusion of hybrid aggregates of the less cohesive ϕ = 48% cell line (Fig. 5a) and of the more cohesive ϕ = 100% cell line for two slightly different MP concentrations (Fig. 5c,e). Fig. 5b,d,f shows log a as a function of log t, which can be fitted with a straight line, and Fig. 5g-i shows a^3/R^2 versus t. The fitted values of the parameter are presented in Table 2, and they are in agreement with the viscoelastic model.

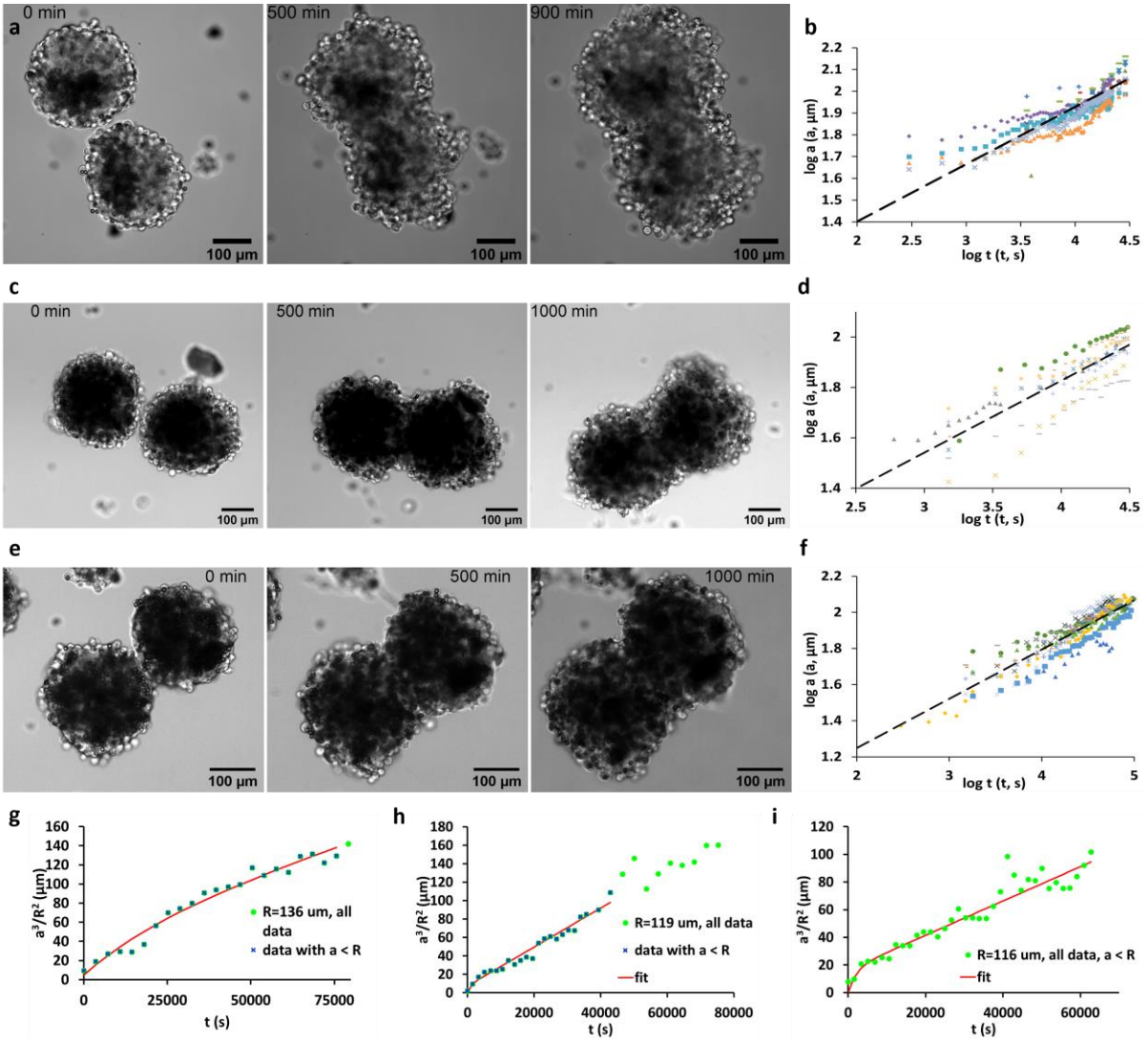

Fig 5. Fusion of cell aggregates with MPs. (a) Snapshots of the fusion of a pair of cell aggregates at t = 0, 500 and 1000 min with ϕ = 48% and φ = 0.06. (b) Plot of log a as a function of log t for cell aggregates with ϕ = 48% and φ = 0.06, n = 11. (c) Snapshots of the fusion of a pair of cell aggregates at t = 0, 500 and 1000 min with ϕ = 100% and φ = 0.10. (d) Plot of log a as a function of log t for cell aggregates with ϕ = 100% and φ = 0.10, n = 6. (e) Snapshots of the fusion of a pair of cell aggregates at t = 0, 500 and 1000 min with ϕ = 100% and φ = 0.12. (f) Plot of log a as a function of log t for cell aggregates with ϕ = 100% and φ = 0.12, n = 10. Doted lines correspond to linear fits. (g) Plot of a^3 / R^2 as a function of t for cell aggregates with ϕ = 48% and φ = 0.06 and theoretical fit using Eq. 15. (h) Plot of a^3 / R^2 as a function of t for cell aggregates with ϕ = 100% and φ = 0.10 and theoretical fit using Eq. (15). (i) Plot of a^3 / R^2 as a function of t of cell aggregates with ϕ = 100% and φ = 0.12 and theoretical fit using Eq. 15.

- Asymmetric fusion of a cellular aggregate with a hybrid aggregate.

Fig. 6 and 7 show the axisymmetric fusion between a homogeneous cellular aggregate and a hybrid cell-MP aggregate. Both aggregates are produced using the same cell line, ϕ = 100%. We visualize the phenomenon both in bright field (Fig. 6a-f, Fig. 7c,f) and using confocal microscopy (Fig. 7a,b,d,e). Fig. 6g and 6h show log a and a^3/R^2 as a function of log t and of t. The values obtained from the fit with the viscoelastic model, shown in Table 2, do not indicate a significant difference in the dynamics of fusion with respect with the symmetric case discussed above. Interestingly, this experiment allows us to monitor how cells mix during fusion. During the first few hours of fusion, the distribution of the particles is not homogeneous and the vast majority of the MPs stay in the initially hybrid aggregate, with few migrating into the initially particle free aggregate. This behavior starkly differs from observations of low viscosity liquids, where a coalesced state of liquid drops is characterized by a complete mixing of molecules, which is not the case here. The slow mixing of the components of the cell aggregates is confirmed by confocal microscopy, where a sharp boundary of MPs can be observed between the fusing aggregates. At long times, the particles internalized inside the cells slowly interdiffuse across the interfaces as shown in Fig. 5f, reflecting the slow diffusion coefficient of the cells in aggregates. We can estimate the interdiffusion coefficient D from Fig. 6f. If x~50 μm is the interpenetration distance after t = 2 days, $D \sim \frac{50^2}{2.24.3600} = 1.4\ 10^{-2}$ μm^2 s^{-1}. This value is an order of magnitude larger to that measured in embryonic tissues[55]. This difference can be attributed to the absence of extracellular matrix in S180 lines, which do not secret it.

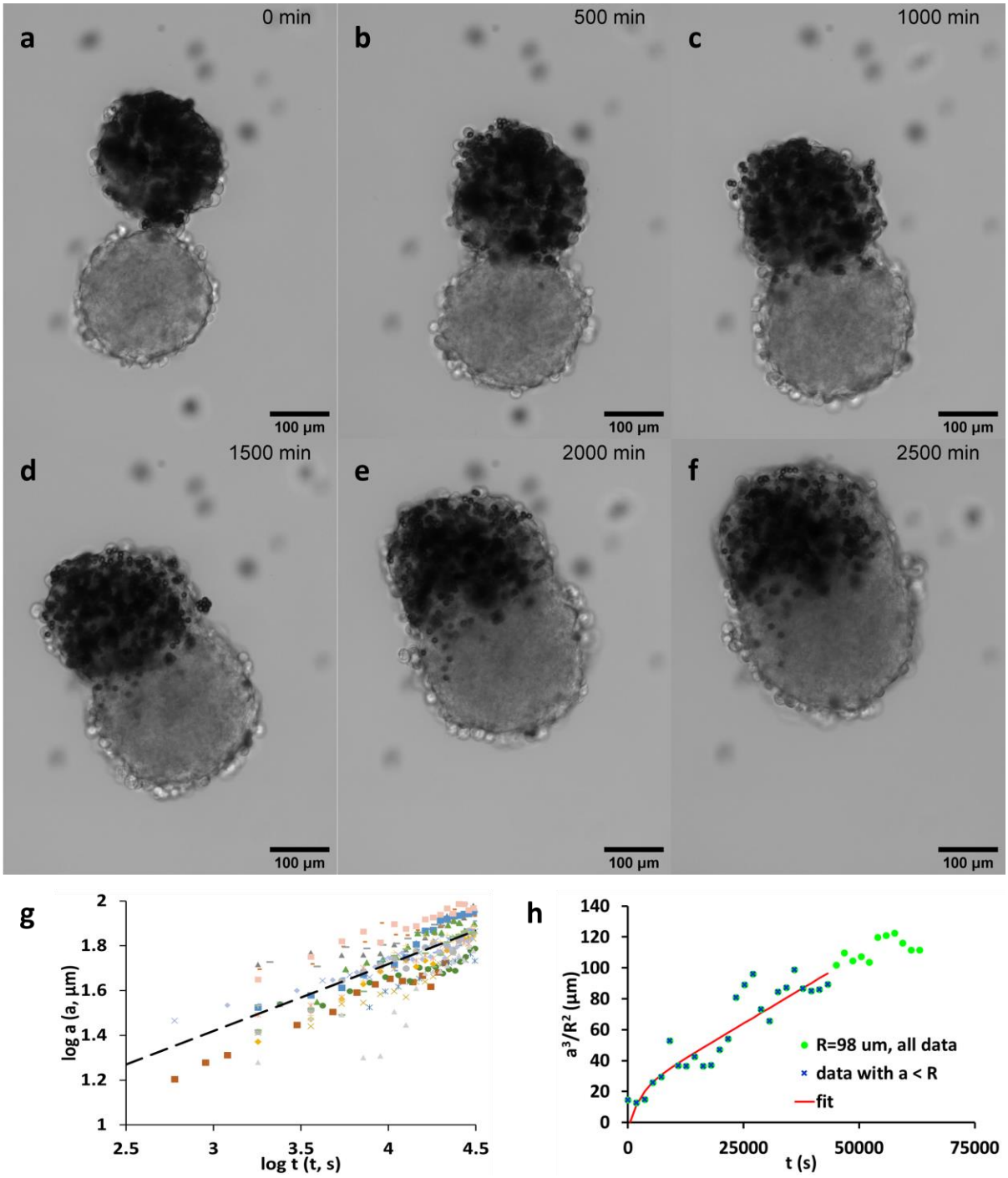

Fig 6. Asymmetric fusion of cellular aggregates. Snapshots of the asymmetric fusion of a pair of cell aggregates with ϕ = 100%, φ = 0 and φ = 0.12 at different times (a) 0 min, (b) 500 min, (c) 1000 min, (d) 1500 min, (e) 2000 min, and (f) 2500 min. (g) Plot of log a as a function of log t for asymmetric fusions, n = 19. The dotted line corresponds to a linear fit. (h) Plot of a^3 / R^2 as a function of t and theoretical fit using Eq. 15.

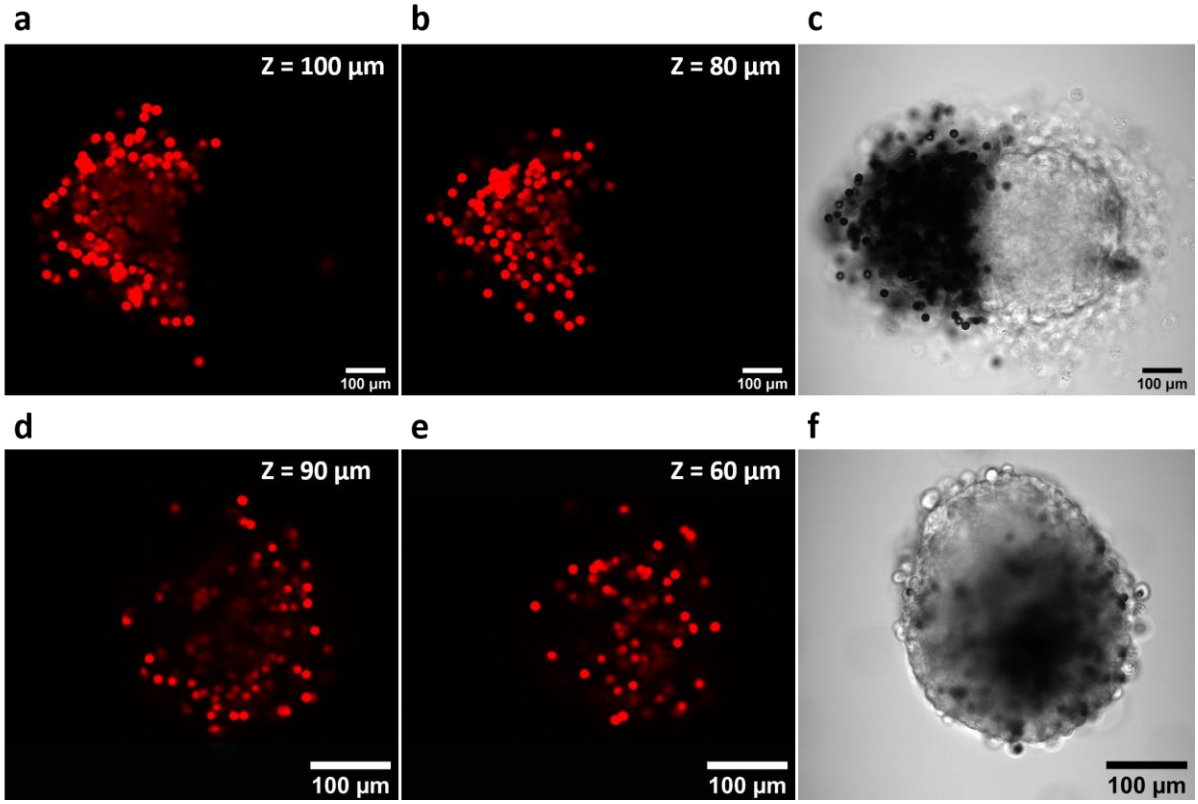

Fig 7. Confocal microscopy of asymmetric fusions. Snapshots of the asymmetric fusion of a pair of cell aggregates with ϕ = 100%, φ = 0 and φ = 0.12 (a-c) at t = 1 day (a) with a confocal microscope at Z = 100 µm, (b) with a confocal microscope at Z = 80 µm, (c) in bright field. (d-f) at t = 2 days (d) by confocal microscopy at Z = 90 µm, (e) by confocal microscopy at Z = 60 µm, (f) in bright field. MPs are visible in red.

Table 2. Main parameters obtained from the fusion analysis for the different types of aggregates.

E-cadherin expression ϕ (%)	MPs in aggregates φ	p	q	L_e (µm)	$V_f^* = \frac{L_e}{\tau_t}$ (µm s^{-1})
48	0 [a]	0.25 ± 0.08 (n=14)	0.91 ± 0.35	28 ± 3 (n=4)	(2.8 ± 0.9).10^{-3} (n=11)
48	about 0.06 [a]	0.25 ± 0.08 (n=11)	0.91 ± 0.32	44 ± 26 (n=4)	(2.1 ± 1.3).10^{-3} (n=14)
100	0 [a]	0.40 ± 0.09 (n=15)	0.19 ± 0.41	8 ± 5 (n=3)	(2.2 ± 0.7).10^{-3} (n=14)
100	0.10 [a]	0.29 ± 0.06 (n=8)	0.67 ± 0.29	17 ± 6 (n=4)	(1.8 ± 0.4).10^{-3} (n=8)
100	0.12 [a]	0.27 ± 0.06 (n=11)	0.70 ± 0.26	9 ± 9 (n=5)	(2.0 ± 0.4).10^{-3} (n=11)

100	0.12 and 0 [b]	0.35 ± 0.07 (n=19)	0.31 ± 0.37	13 ± 4 (n=6)	$(1.4 \pm 0.6).10^{-3}$ (n=19)

[a] symmetric fusions

[b] asymmetric fusions

5. Conclusion

Our studies on the fusion of homogeneous cellular aggregates and of hybrid aggregates containing microparticles have shown that the contact area as a function of time does not vary linearly as observed for liquid drops, but rather it follows a power law in $t^{2/3}$. Our experimental results have been interpreted by a viscoelastic liquid drop fusion model, which is an extension of the viscoelastic soft solid fusion model that was previously derived to describe adhesion of inert elastomers. Our proposed model involves a characteristic elastic length L_e, which describes the competition between the deformation energy of the soft matrix and the surface energy, and a characteristic fusion velocity V_f^*.

L_e is the ratio of the surface tension divided by the elastic modulus measured at short times. The values obtained for L_e range from a few microns to tens of microns. Because the accuracy of the measure of the radius a of the neck is limited by the cell size, the uncertainty of our L_e estimates is high. To experimentally characterize the short-time elastic regime described by our model, for which our current data are scarce, it will be interesting to extend our work to the fusion of soft brain tissues or to ultraviscous liquids, characterized by larger L_e values. The fusion velocity V_f^* is proportional to the ratio between the aggregate surface tension and the tissue viscosity. Our values for V_f^* are in the range of $(2 \pm 1).10^{-3}$ µm s^{-1}.

Most previous studies on the fusion of cellular aggregates have described the fusion using the classic viscous liquid model. Thus, they fitted a linear law to the evolution of the contact area over time, instead of the $t^{2/3}$ exponent found here for a viscoelastic material. This discrepancy may be explained by the relatively small difference between the two exponents, even if the linear exponent is outside our experimentally deduced confidence intervals. The discrepancy could also be due to different behaviors of different cell types. For example, we expect that the presence of an extracellular matrix, which is absent in our aggregates, will significantly affect the fusion dynamics.

We have investigated how aggregate fusion depends on E-cadherin expression and on the presence of microparticles inside the aggregates. Variation of E-cadherin expression by a factor of 2 has a minor effect on the fusion dynamics, and the fusion velocity V_f^* remains comparable.

Since the fusion velocity is a ratio between intercellular adhesion and tissue viscosity, we deduce that these two factors increase proportionally to each other with increasing E-cadherin expression. Indeed, we expect cell-cell adhesion to be proportional to cadherin expression, and viscosity is also proportional to it, as it has been previously reported.[8] Adding microparticles to the aggregates reduces their fusion velocity, an observation consistent with the slowdown of aggregate spreading in the presence of particles, reported previously.[53]

In the case of asymmetric fusion, we have been able to follow the dynamics of interpenetration of the two aggregates. It has been reported that aggregates fuse, but do not mix as regular liquids. We have shown that the interpenetration is very slow. We have been able to measure the diffusion coefficient of a cell in the aggregate and found $D \approx 1.4\,10^{-2}$ μm^2 s^{-1}. This experimental setup constitutes a novel and relatively easy method to measure such an extremely small diffusion coefficient.

Supporting information.

Supplementary Table 1. Cell division of cells during the formation of aggregates in pendant droplets.

Supplementary Table 2. Main parameters obtained from the fusion analysis up to log t = 4.5.

7. Acknowledgments

This work was supported by the Academy of Finland Center of Excellence Programme (2014–2019).

8. References

(1) Gonzalez-Rodriguez, D.; Guevorkian, K.; Douezan, S.; Brochard-Wyart, F. Soft Matter Models of Developing Tissues and Tumors. *Science* **2012**, *338* (6109), 910–917. https://doi.org/10.1126/science.1226418.

(2) Sart, S.; Tsai, A. C.; Li, Y.; Ma, T. Three-Dimensional Aggregates of Mesenchymal Stem Cells: Cellular Mechanisms, Biological Properties, and Applications. *Tissue Engineering - Part B: Reviews*. Mary Ann Liebert, Inc. 140 Huguenot Street, 3rd Floor New Rochelle, NY 10801 USA December 2014, pp 365–380. https://doi.org/10.1089/ten.teb.2013.0537.

(3) Verhulsel, M.; Vignes, M.; Descroix, S.; Malaquin, L.; Vignjevic, D. M.; Viovy, J. L. A Review of Microfabrication and Hydrogel Engineering for Micro-Organs on Chips. *Biomaterials*. Elsevier February 2014, pp 1816–1832. https://doi.org/10.1016/j.biomaterials.2013.11.021.

(4) Steinberg, M. S. Reconstruction of Tissues by Dissociated Cells. *Sci. Sci.* **1963**, *141* (3579), 401–408. https://doi.org/10.1126/science.141.3579.401.

(5) Steinberg, M. S. Does Differential Adhesion Govern Self-assembly Processes in Histogenesis? Equilibrium Configurations and the Emergence of a Hierarchy among Populations of Embryonic Cells. *J. Exp. Zool.* **1970**, *173* (4), 395–433. https://doi.org/10.1002/jez.1401730406.

(6) Preziosi, L.; Ambrosi, D.; Verdier, C. An Elasto-Visco-Plastic Model of Cell Aggregates. *J. Theor. Biol.* **2010**, *262* (1), 35–47. https://doi.org/10.1016/j.jtbi.2009.08.023.

(7) Tlili, S.; Gay, C.; Graner, F.; Marcq, P.; Molino, F.; Saramito, P. Colloquium: Mechanical Formalisms for Tissue Dynamics. *European Physical Journal E*. Springer May 2015, pp 1–31. https://doi.org/10.1140/epje/i2015-15033-4.

(8) Douezan, S.; Guevorkian, K.; Naouar, R.; Dufour, S.; Cuvelier, D.; Brochard-Wyart, F. Spreading Dynamics and Wetting Transition of Cellular Aggregates. *Proc. Natl. Acad. Sci. U. S. A.* **2011**, *108* (18), 7315–7320. https://doi.org/10.1073/pnas.1018057108.

(9) Beaune, G.; Stirbat, T. V.; Khalifat, N.; Cochet-Escartin, O.; Garcia, S.; Gurchenkov, V. V.; Murrell, M. P.; Dufour, S.; Cuvelier, D.; Brochard-Wyart, F. How Cells Flow in the Spreading of Cellular Aggregates. *Proc. Natl. Acad. Sci.* **2014**, *111* (22), 8055–8060. https://doi.org/10.1073/pnas.1323788111.

(10) Guevorkian, K.; Colbert, M.-J.; Durth, M.; Dufour, S.; Brochard-Wyart, F. Aspiration of Biological Viscoelastic Drops. *Phys. Rev. Lett.* **2010**, *104* (21), 218101. https://doi.org/10.1103/PhysRevLett.104.218101.

(11) Guevorkian, K.; Maître, J. L. Micropipette Aspiration: A Unique Tool for Exploring Cell and Tissue Mechanics in Vivo. *Methods Cell Biol.* **2017**, *139*, 187–201. https://doi.org/10.1016/bs.mcb.2016.11.012.

(12) Stirbat, T. V.; Mgharbel, A.; Bodennec, S.; Ferri, K.; Mertani, H. C.; Rieu, J.-P.; Delanoë-Ayari, H. Fine Tuning of Tissues' Viscosity and Surface Tension through Contractility Suggests a New Role for α-Catenin. *PLoS One* **2013**, *8* (2), e52554. https://doi.org/10.1371/journal.pone.0052554.

(13) Forgacs, G.; Foty, R. A.; Shafrir, Y.; Steinberg, M. S. Viscoelastic Properties of Living Embryonic Tissues: A Quantitative Study. *Biophys. J.* **1998**, *74* (5), 2227–2234. https://doi.org/10.1016/S0006-3495(98)77932-9.

(14) Pérez-Pomares, J. M.; Foty, R. A. Tissue Fusion and Cell Sorting in Embryonic Development and Disease: Biomedical Implications. *BioEssays*. Bioessays August 2006, pp 809–821. https://doi.org/10.1002/bies.20442.

(15) Jakab, K.; Neagu, A.; Mironov, V.; Markwald, R. R.; Forgacs, G. Engineering Biological Structures of Prescribed Shaped Using Self-Assembling Multicellular Systems. *Proc. Natl. Acad. Sci. U. S. A.* **2004**, *101* (9), 2864–2869. https://doi.org/10.1073/pnas.0400164101.

(16) Mironov, V.; Visconti, R. P.; Kasyanov, V.; Forgacs, G.; Drake, C. J.; Markwald, R. R. Organ Printing: Tissue Spheroids as Building Blocks. *Biomaterials* **2009**, *30* (12), 2164–2174. https://doi.org/10.1016/j.biomaterials.2008.12.084.

(17) Fleming, P. A.; Argraves, W. S.; Gentile, C.; Neagu, A.; Forgacs, G.; Drake, C. J. Fusion of Uniluminal Vascular Spheroids: A Model for Assembly of Blood Vessels. *Dev. Dyn.* **2010**, *239* (2), 398–406. https://doi.org/10.1002/dvdy.22161.

(18) Frenkel, J. Viscous Flow of Crystalline Bodies under the Action of Surface Tension. *J*

Phys Moscow **1945**, *9*, 85.

(19) Ristic, M.; Milosevic, S. D. Frenkel's Theory of Sintering. *Sci. Sinter.* **2006**, *38* (1), 7–11. https://doi.org/10.2298/SOS0601007R.

(20) Shaler, A. Seminar on the Kinetics of Sintering. *Met. Trans* **1949**, *185* (11), 796–813.

(21) Pokluda, O.; Bellehumeur, C. T.; Vlachopoulos, J. Modification of Frenkel's Model for Sintering. *AIChE J.* **1997**, *43* (12), 3253–3256. https://doi.org/10.1002/aic.690431213.

(22) Hopper, R. W. Plane Stokes Flow Driven by Capillarity on a Free Surface. *J. Fluid Mech.* **1990**, *213*, 349–375. https://doi.org/10.1017/S002211209000235X.

(23) Jagota, A.; Dawson, P. R. Simulation of the Viscous Sintering of Two Particles. *J. Am. Ceram. Soc.* **1990**, *73* (1), 173–177. https://doi.org/10.1111/j.1151-2916.1990.tb05117.x.

(24) van de Vorst, G. A. L. Numerical Simulation of Axisymmetric Viscous Sintering. *Eng. Anal. Bound. Elem.* **1994**, *14* (2), 193–207. https://doi.org/10.1016/0955-7997(94)90096-5.

(25) Martínez-Herrera, J. I.; Derby, J. J. Viscous Sintering of Spherical Particles via Finite Element Analysis. *J. Am. Ceram. Soc.* **1995**, *78* (3), 645–649. https://doi.org/10.1111/j.1151-2916.1995.tb08226.x.

(26) Zhou, H.; Derby, J. J. Three-Dimensional Finite-Element Analysis of Viscous Sintering. *J. Am. Ceram. Soc.* **1998**, *81* (3), 533–540. https://doi.org/10.1111/j.1151-2916.1998.tb02371.x.

(27) Johnson, K. L.; Kendall, K.; Roberts, A. D. Surface Energy and the Contact of Elastic Solids. *Proc. R. Soc. London. A. Math. Phys. Sci.* **1971**, *324* (1558), 301–313. https://doi.org/10.1098/rspa.1971.0141.

(28) Michel, F.; Shanahan, M. E. R. Kinetics of the JKR Experiment. *COMPTES RENDUS L Acad. DES Sci. Ser. II* **1990**, *310* (1), 17–20.

(29) Bellehumeur, C. T.; Bisaria, M. K.; Vlachopoulos, J. An Experimental Study and Model Assessment of Polymer Sintering. *Polym. Eng. Sci.* **1996**, *36* (17), 2198–2207. https://doi.org/10.1002/pen.10617.

(30) Bellehumeur, C. T.; Kontopoulou, M.; Vlachopoulos, J. The Role of Viscoelasticity in Polymer Sintering. *Rheol. Acta* **1998**, *37* (3), 270–278. https://doi.org/10.1007/s003970050114.

(31) Mazur, S.; Plazek, D. J. Viscoelastic Effects in the Coalescence of Polymer Particles. *Prog. Org. Coatings* **1994**, *24* (1–4), 225–236. https://doi.org/10.1016/0033-0655(94)85016-X.

(32) Jagota, A.; Argento, C.; Mazur, S. Growth of Adhesive Contacts for Maxwell Viscoelastic Spheres. *J. Appl. Phys.* **1998**, *83* (1), 250–259. https://doi.org/10.1063/1.366679.

(33) Hooper, R.; Macosko, C. W.; Derby, J. J. Assessing a Flow-Based Finite Element Model for the Sintering of Viscoelastic Particles. *Chem. Eng. Sci.* **2000**, *55* (23), 5733–5746. https://doi.org/10.1016/S0009-2509(00)00224-4.

(34) Scribben, E.; Baird, D.; Wapperom, P. The Role of Transient Rheology in Polymeric Sintering. *Rheol. Acta* **2006**, *45* (6), 825–839. https://doi.org/10.1007/s00397-005-0039-1.

(35) Balemans, C.; Hulsen, M. A.; Anderson, P. D. Sintering of Two Viscoelastic Particles: A Computational Approach. *Appl. Sci.* **2017**, *7* (5), 516. https://doi.org/10.3390/app7050516.

(36) David, R.; Luu, O.; Damm, E. W.; Wen, J. W. H.; Nagel, M.; Winklbauer, R. Tissue Cohesion and the Mechanics of Cell Rearrangement. *Dev.* **2014**, *141* (19), 3672–3682. https://doi.org/10.1242/dev.104315.

(37) Gordon, R.; Goel, N. S.; Steinberg, M. S.; Wiseman, L. L. A Rheological Mechanism Sufficient to Explain the Kinetics of Cell Sorting. *J. Theor. Biol.* **1972**, *37* (1), 43–73. https://doi.org/10.1016/0022-5193(72)90114-2.

(38) Jakab, K.; Damon, B.; Marga, F.; Doaga, O.; Mironov, V.; Kosztin, I.; Markwald, R.; Forgacs, G. Relating Cell and Tissue Mechanics: Implications and Applications. *Dev. Dyn.* **2008**, *237* (9), 2438–2449. https://doi.org/10.1002/dvdy.21684.

(39) EM, S.; RD, B.; F, J.; MS, S.; CP, H.; RA, F. Quantitative Differences in Tissue Surface Tension Influence Zebrafish Germ Layer Positioning. *HFSP J.* **2008**, *2* (1), 42–56. https://doi.org/10.2976/1.2834817.

(40) Douezan, S.; Brochard-Wyart, F. Active Diffusion-Limited Aggregation of Cells. *Soft Matter* **2012**, *8* (3), 784. https://doi.org/10.1039/c1sm06399e.

(41) Flenner, E.; Janosi, L.; Barz, B.; Neagu, A.; Forgacs, G.; Kosztin, I. Kinetic Monte Carlo and Cellular Particle Dynamics Simulations of Multicellular Systems. *Phys. Rev. E - Stat. Nonlinear, Soft Matter Phys.* **2012**, *85* (3), 031907. https://doi.org/10.1103/PhysRevE.85.031907.

(42) Dechristé, G.; Fehrenbach, J.; Griseti, E.; Lobjois, V.; Poignard, C. Viscoelastic Modeling of the Fusion of Multicellular Tumor Spheroids in Growth Phase. *J. Theor. Biol.* **2018**, *454*, 102–109. https://doi.org/10.1016/j.jtbi.2018.05.005.

(43) Oriola, D.; Marin-Riera, M.; Aalderink, G.; Anlas, K.; Gritti, N.; Sharpe, J.; Trivedi, V. Arrested Coalescence of Multicellular Aggregates. *arXiv Prepr. arXiv2012.01455* **2020**.

(44) Ongenae, S.; Cuvelier, M.; Vangheel, J.; Ramon, H.; Smeets, B. Activity-Induced Fluidization and Arrested Coalescence in Fusion of Cellular Aggregates. *Front. Phys.* **2021**, *9*, 321. https://doi.org/10.3389/fphy.2021.649821.

(45) Tsai, A. C.; Liu, Y.; Yuan, X.; Ma, T. Compaction, Fusion, and Functional Activation of Three-Dimensional Human Mesenchymal Stem Cell Aggregate. *Tissue Eng. - Part A* **2015**, *21* (9–10), 1705–1719. https://doi.org/10.1089/ten.tea.2014.0314.

(46) Pierzchalska, M.; Panek, M.; Grabacka, M. The Migration and Fusion Events Related to ROCK Activity Strongly Influence the Morphology of Chicken Embryo Intestinal Organoids. *Protoplasma* **2019**, *256* (2), 575–581. https://doi.org/10.1007/s00709-018-1312-3.

(47) Grosser, S.; Lippoldt, J.; Oswald, L.; Merkel, M.; Sussman, D. M.; Renner, F.; Gottheil, P.; Morawetz, E. W.; Fuhs, T.; Xie, X.; others. Cell and Nucleus Shape as an Indicator of Tissue Fluidity in Carcinoma. *Phys. Rev. X* **2021**, *11* (1), 11033.

(48) Kosheleva, N. V.; Efremov, Y. M.; Shavkuta, B. S.; Zurina, I. M.; Zhang, D.; Zhang, Y.; Minaev, N. V.; Gorkun, A. A.; Wei, S.; Shpichka, A. A.; Saburina, I. N.; Timashev, P. S. Cell Spheroid Fusion: Beyond Liquid Drops Model. *Sci. Rep.* **2020**, *10* (1), 1–15. https://doi.org/10.1038/s41598-020-69540-8.

(49) Murrell, M.; Pontani, L.-L.; Guevorkian, K.; Cuvelier, D.; Nassoy, P.; Sykes, C.

Spreading Dynamics of Biomimetic Actin Cortices. *Biophys. J.* **2011**, *100* (6), 1400–1409. https://doi.org/10.1016/j.bpj.2011.01.038.

(50) Cuvelier, D.; Théry, M.; Chu, Y.-S.; Dufour, S.; Thiéry, J.-P.; Bornens, M.; Nassoy, P.; Mahadevan, L. The Universal Dynamics of Cell Spreading. *Curr. Biol.* **2007**, *17* (8), 694–699. https://doi.org/10.1016/j.cub.2007.02.058.

(51) Odenthal, T.; Smeets, B.; Van Liedekerke, P.; Tijskens, E.; Van Oosterwyck, H.; Ramon, H. Analysis of Initial Cell Spreading Using Mechanistic Contact Formulations for a Deformable Cell Model. *PLoS Comput. Biol.* **2013**, *9* (10), e1003267. https://doi.org/10.1371/journal.pcbi.1003267.

(52) Chu, Y.-S.; Thomas, W. A.; Eder, O.; Pincet, F.; Perez, E.; Thiery, J. P.; Dufour, S. Force Measurements in E-Cadherin-Mediated Cell Doublets Reveal Rapid Adhesion Strengthened by Actin Cytoskeleton Remodeling through Rac and Cdc42. *J. Cell Biol.* **2004**, *167* (6), 1183–1194. https://doi.org/10.1083/jcb.200403043.

(53) Nagarajan, U.; Beaune, G.; Lam, A. Y. W.; Gonzalez-Rodriguez, D.; Winnik, F. M.; Brochard-Wyart, F. Inert-Living Matter, When Cells and Beads Play Together. *Commun. Phys.* **2021**, *4* (1), 2. https://doi.org/10.1038/s42005-020-00506-y.

(54) De Gennes, P.-G.; Brochard-Wyart, F.; Quere, D. *Capillary and Wetting Phenomena : Bubbles, Drops, Pearls, Waves.*, Springer.; 2004.

(55) Mombach, J. C. M.; Glazier, J. A. Single Cell Motion in Aggregates of Embryonic Cells. *Phys. Rev. Lett.* **1996**, *76* (16), 3032–3035. https://doi.org/10.1103/PhysRevLett.76.3032.

Supporting Information

Fusion Dynamics of Hybrid Cell-Microparticles Aggregates: A Jelly Pearl Model

Grégory Beaune,[1] Laura Sinkonen,[1] David Gonzalez-Rodriguez,[2,#] Jaakko V.I. Timonen,[1,#] Françoise Brochard-Wyart[3,#,*]

[1] Department of Applied Physics, Aalto University School of Science, 02150 Espoo, Finland

[2] Université de Lorraine, LCP-A2MC, F-57000, Metz, France

[3] Institut Curie, Université PSL, Sorbonne Université, CNRS UMR168, Laboratoire Physico Chimie Curie, 75005, Paris, France

[#] Equally contributors

*Corresponding author. Email: Francoise.Brochard@curie.fr

Supplementary Table 1. Cell Division During the Formation of Aggregates in Pendant Droplets

E-cadherin expression ϕ (%)	Initial no. of cells/droplet, N_i	No. of cells/aggregate before fusion, N_f	N_f / N_i
48	1100	5400	4.9 (n = 28)
100	1000	4300	4.3 (n = 30)

Supplementary Table 2. Main Parameters Obtained from the Fusion Analysis for the Different Types of Aggregates up to log t = 4.5

E-cadherin expression ϕ (%)	Volume fraction of MPs in aggregates	p	q
48	0[a]	0.26 ± 0.09 (n = 14)	0.87 ± 0.40
48	about 0.06[a]	0.27 ± 0.12 (n = 11)	0.87 ± 0.52
100	0[a]	0.41 ± 0.15 (n = 15)	0.11 ± 0.62
100	0.10[a]	0.29 ± 0.06 (n = 8)	0.68 ± 0.27
100	0.12[a]	0.26 ± 0.08 (n = 11)	0.74 ± 0.35
100	0.12 and 0[b]	0.30 ± 0.08 (n = 19)	0.52 ± 0.37

[a] Symmetric fusions [b] Asymmetric fusions